Direct Comparisons between GPM-DPR and *CloudSat* Snowfall Retrievals

RANDY J. CHASE,[a] STEPHEN W. NESBITT,[a] GREG M. MCFARQUHAR,[b,c] NORMAN B. WOOD,[d] AND GERALD M. HEYMSFIELD[e]

[a] *Department of Atmospheric Sciences, University of Illinois at Urbana–Champaign, Urbana, Illinois*
[b] *School of Meteorology, University of Oklahoma, Norman, Oklahoma*
[c] *Cooperative Institute for Severe and High-Impact Weather Research and Operations, University of Oklahoma, Norman, Oklahoma*
[d] *Space Science and Engineering Center, University of Wisconsin–Madison, Madison, Wisconsin*
[e] *NASA Goddard Space Flight Center, Greenbelt, Maryland*

(Manuscript received 26 April 2021, in final form 14 May 2022)

ABSTRACT: Two spaceborne radars currently in orbit enable the sampling of snowfall near the surface and throughout the atmospheric column, namely, *CloudSat*'s Cloud Profiling Radar (CPR) and the Global Precipitation Measurement mission's Dual-Frequency Precipitation Radar (GPM-DPR). In this paper, a direct comparison of the CPR's 2C-SNOW-PROFILE (2CSP), the operational GPM-DPR algorithm (2ADPR) and a neural network (NN) retrieval applied to the GPM-DPR data is performed using coincident observations between both radars. Examination of over 3500 profiles within moderate to strong precipitation (Ka band $\geq$ 18 dBZ) show that the NN retrieval provides the closest retrieval of liquid equivalent precipitation rate R immediately above the melting level to the R retrieved just below the melting layer, agreeing within 5%. Meanwhile, 2CSP retrieves a maximum value of R at −15°C, decreases by 35% just above the melting layer, and is about 50% smaller than the GPM-DPR retrieved R below the melting layer. CPR-measured reflectivity shows median reduction of 2–3 dB from −15° to −2.5°C, likely the reason for the 2CSP retrieval reduction of R. Two case studies from NASA field campaigns [i.e., Olympic Mountains Experiment (OLYMPEX) and Investigation of Microphysics and Precipitation for Atlantic Coast-Threatening Snowstorms (IMPACTS)] provide analogs to the type of precipitating systems found in the comparison between retrieval products. For the snowfall events that GPM-DPR can observe, this work suggests that the 2CSP retrieval is likely underestimating the unattenuated reflectivity, resulting in a potential negative, or low, bias in R. Future work should investigate how frequently the underestimated reflectivity profiles occur within the CPR record and quantify its potential effects on global snowfall accumulation estimation.

KEYWORDS: Atmosphere; Ice crystals; Ice particles; Radars/radar observations; Remote sensing; Satellite observations

1. Introduction

Most of the world's precipitation falls as rain, but more than half can be related to ice processes found aloft (Field and Heymsfield 2015; Heymsfield et al. 2020). Thus, any attempt to fully quantify the hydrological cycle must include solid-phase hydrometeor processes and measurements. Furthermore, the amount of snow that falls to the surface is vital in mountainous regions where humanity relies on the melted runoff as their main freshwater resource (e.g., Viviroli et al. 2003). One method of quantifying characteristics of solid-phase hydrometeors is the use of radar. Currently there are two satellites in orbit carrying meteorological radars capable of quantifying global precipitation characteristics, *CloudSat* and the Global Precipitation Measurement (GPM) mission *Core Observatory*.

CloudSat was launched in 2006 carrying the Cloud Profiling Radar (CPR), a nonscanning 94-GHz radar in a 98° sun-synchronous orbit (Stephens et al. 2002; Tanelli et al. 2008). The operating frequency, high sensitivity, and relatively small instantaneous field of view (IFOV) allows successful detection of most clouds found in the troposphere. Since 2006, CPR has been used for numerous global snowfall studies (Liu 2009; Kulie and Bennartz 2009; Palerme et al. 2014; Kulie et al. 2016; Palerme et al. 2017; Milani et al. 2018; Kulie and Milani 2018; Kulie et al. 2020), and after evaluation against several ground-based methods (e.g., Cao et al. 2014; Norin et al. 2015; Chen et al. 2016; Souverijns et al. 2018; Matrosov 2019), CPR has become commonly used as a global snowfall reference (e.g., Palerme et al. 2017; Milani et al. 2018; Skofronick-Jackson et al. 2019; Cabaj et al. 2020; Edel et al. 2020).

The GPM *Core Observatory* was launched in 2014 into a 65° non-sun-synchronous orbit carrying the scanning Dual-

Chase's current affiliations: School of Computer Science, School of Meteorology, and NSF AI Institute for Research on Trustworthy AI in Weather, Climate, and Coastal Oceanography, University of Oklahoma, Norman, Oklahoma.

Corresponding author: Randy J. Chase, randychase@ou.edu

DOI: 10.1175/JAMC-D-21-0081.1

Frequency Precipitation Radar (DPR) operating at 13.5 and 35.5 GHz (Hou et al. 2014). Contrary to *CloudSat*, GPM-DPR has a relatively large IFOV and a more limited sensitivity, thus GPM-DPR is generally more useful for moderate to intense precipitation. Despite GPM-DPR's limitations, the radar has been used for global snowfall studies (Adhikari et al. 2018; Adhikari and Liu 2019).

The comparison of CPR, GPM-DPR, and their operational retrieval products, namely, the 2C-SNOW-PROFILE from *CloudSat* (Wood and L'Ecuyer 2018, 2021) and the 2ADPR from GPM-DPR (Iguchi et al. 2018; Seto et al. 2021), shows that the 2ADPR near-surface snowfall retrieval product is negatively (hereinafter "low") biased (Casella et al. 2017; Tang et al. 2017; Skofronick-Jackson et al. 2019). Casella et al. (2017) used a coincident database of CPR and GPM-DPR observations (Turk 2016; Turk et al. 2021) and found that more than 90% of near-surface snowfall events by number are missed by GPM-DPR, attributing this to GPM-DPR's lack of sensitivity. However, Casella et al. (2017) state that while GPM-DPR is missing a large fraction of events by number, the fraction of the snowfall accumulation captured by GPM-DPR is estimated to be around 30% of the total global snowfall accumulation. Skofronick-Jackson et al. (2019) compared three years of CPR and GPM-DPR measurements statistically, accounting for hardware, retrieval algorithm, and operating frequency differences. After careful quality control, it was found that on a global average GPM-DPR near-surface snowfall accumulation was about 43% lower than CPR, but the disparity can be larger at specific locations by up to 800 mm yr^{-1} (Skofronick-Jackson et al. 2019). Motivated by the work of Casella et al. (2017) and Skofronick-Jackson et al. (2019), Chase et al. (2020) investigated the microphysical assumptions within the 2ADPR retrieval algorithm and found that the assumed empirical parameterization between the liquid equivalent mass flux R and the liquid equivalent mass-weighted mean diameter D_m does not characterize surface snowfall observations well and contributes to the low bias reported in Skofronick-Jackson et al. (2019). Following the work of Chase et al. (2020), Chase et al. (2021) developed an alternative dual-frequency retrieval for GPM-DPR that shows initially good performance against in situ observations, with a median bias of 13%, 120%, and 10% for D_m, the liquid equivalent normalized intercept parameter N_w, and ice water content (IWC), respectively. Chase et al. (2021) also showed that their retrieval implemented on the GPM-DPR measurements removes along track ray-to-ray instabilities found in the current 2ADPR method (cf. Fig. 15 in Chase et al. 2021).

The primary goal of this paper is to evaluate the new retrieval method developed for GPM-DPR by Chase et al. (2021) directly against CPR's 2C-SNOW-PROFILE retrieval. Secondary goals of this paper are to quantify and discuss the potential limitations of W-band single-frequency retrievals in context of moderate to intense snowfall events as well as evaluate the operational 2ADPR snowfall retrieval against the 2C-SNOW-PROFILE. Although CPR's 2C-SNOW-PROFILE has shown generally good agreement with ground-based sensors (e.g., Cao et al. 2014; Norin et al. 2015; Chen et al. 2016; Souverijns et al. 2018; Matrosov 2019) there have been indications that the 2C-SNOW-PROFILE retrieval is low biased relative to other snow accumulation measurements. For example, Ryan et al. (2020) showed that 2C-SNOW-PROFILE is low relative to ice core estimates over Greenland. Further, Cao et al. (2014) and Mróz et al. (2021) showed for moderate to intense snowfall rates (>1 mm h^{-1}) 2C-SNOW-PROFILE underestimates the S-band radar snowfall. The rest of this paper is structured as follows: section 2 discusses the retrieval methods, the coincident dataset between GPM-DPR and CPR, the quality control methods used to ensure a consistent comparison of GPM-DPR and CPR, and information on the field campaign datasets used. Section 3 contains the results, starting with the statistical comparison between snowfall products on the coincident dataset, and then discussing the snowfall product comparison in context of two cases studies from NASA field campaigns. Section 4 summarizes the main results, conclusions, and future directions of research.

2. Methods

a. Retrieval methods

2C-SNOW-PROFILE (2CSP), uses optimal estimation (Rodgers 2000) to retrieve profiles of the two parameters of the exponential particle size distribution based on a state vector containing the gaseous attenuation corrected W-band reflectivity profile supplemented with coincident environmental conditions from ECMWF High-Resolution Forecast simulations and a priori characteristics of snow (Wood and L'Ecuyer 2018, 2021). From the two parameters of the size distribution and a few assumptions, snowfall properties such as IWC and R can be calculated. For the 2CSP retrieval, the terminal fall velocity relation used is pressure adjusted, while the 2ADPR (Seto et al. 2013) and the Chase et al. (2021) retrieval using the GPM-DPR data assume that the retrieval is made with a pressure of 1013 hPa. Since the fall speeds of particles, and thus their precipitation rate, is proportional to air pressure (i.e., more air pressure, more drag, lower precipitation rate), the 2CSP retrieval is converted to a retrieval that is assumed to be at 1013 hPa. To convert the 2CSP retrieval, a scale factor is applied to the 2CSP product using the following relation (Brandes et al. 2008):

$$R_{\mathrm{msl}} = R_i\left(\frac{P_i}{1013\,\mathrm{hPa}}\right)^{0.5}, \tag{1}$$

where R_{msl} is the liquid equivalent precipitation rate at mean sea level (1013 hPa), R_i is the precipitation rate at the retrieval level, and P_i is the pressure at the retrieval level. For the rest of the analysis in this paper, the R_{msl} is compared between all retrievals (herein written as R).

The latest version for the GPM-DPR retrieval, version 6 (Iguchi et al. 2018), uses a prescribed relation between R and D_m to simultaneously retrieve R and D_m for a given measured radar reflectivity factor Z_e. The retrieval is done iteratively, varying an adjustment parameter ϵ in the column to minimize the error between the retrieved and estimated path integrated

attenuation and the measured Ka-band Z_e. More details are found in the algorithm theoretical basis document (Iguchi et al. 2018). Overall, the algorithm shows good performance on the retrieval of R and D_m in rain when compared with data collected during NASA's Ground Validation field campaigns, satisfying GPM's level-1 mission requirement of an error of less than 50% and 0.5 mm for R and D_m, respectively (Petersen et al. 2020; Gatlin et al. 2020). Note that the R–D_m retrieval framework is used in all GPM-DPR gates, regardless of hydrometeor phase despite being derived from surface rainfall measurements. Version 6 of the 2ADPR algorithm does make adjustments to some of the assumptions in the scattering tables and the underlying particle size distribution when being used for solid-phase designated radar gates, but the underlying R–D_m relation is exactly the same. The use of the R–D_m parameterization has contributed to the low bias within snowfall retrievals (e.g., Skofronick-Jackson et al. 2019; Chase et al. 2020), but the 2ADPR retrieval for snowfall is included for comparison in section 3a.

As an alternative to the R–D_m retrieval in snowfall using GPM-DPR, a dual-frequency radar neural network retrieval of snowfall parameters formulated by Chase et al. (2021) is also evaluated. The retrieval was built using state-of-the-art particle scattering models (e.g., discrete dipole approximation; Yurkin and Hoekstra 2011) and measured particle size distributions from multiple NASA field campaigns (e.g., Jensen et al. 2016; Skofronick-Jackson et al. 2017; Houze et al. 2017) to inform the weights and biases of a neural network. The Chase et al. (2021) retrieval, neural network (NN), is performed on a gate-by-gate basis and takes inputs of the measured Z_e at Ku band, measured dual-frequency ratio between Ku and Ka band, and the temperature of the radar gate. The retrieval passes the inputs through trained weights and biases, and outputs estimates of D_m and N_w. From D_m and N_w IWC can be calculated following Delanoë et al. (2014):

$$\mathrm{IWC} = \left(\frac{N_w D_m^4 \rho_l \pi}{4^4}\right), \tag{2}$$

where ρ_l is the density of liquid water.

Since the goal of this study is to compare R, some assumptions have to be made to convert the IWC to R within the NN retrieval. To do so, a linear regression between log(R) and log(IWC) is fit using ground-based precipitation imaging package (PIP) measurements acquired at the University of Helsinki Hyytiälä Forestry Field Station in Finland (von Lerber et al. 2017; Chase et al. 2020) and the National Weather Service office in Marquette, Michigan (Pettersen et al. 2020). The PIP data are used because the mass of particles is retrieved from their respective observed fall velocities (cf. von Lerber et al. 2017), thus giving a more constrained estimate of R and IWC from measured particle size distributions. The fit to the empirical relation is given by

$$R = 3.64(\mathrm{IWC})^{1.06} \tag{3}$$

and is shown graphically in Fig. 1. The units for the coefficient of 3.64 in Eq. (3) are $(\mathrm{m^3\ g^{-1}})^{1.06}$ mm $\mathrm{h^{-1}}$. The total PIP dataset includes about 600 h of snowfall measurements, composed of 5-min individual observations. The mean estimated error (i.e., regression R − observed R) from using a linear regression to calculate R from IWC is 0.04 mm $\mathrm{h^{-1}}$. While an empirical relationship, such as the one presented in Eq. (3), can introduce a bias in the NN retrieval, there is added confidence in the fact that deriving the relationship with the two sites independently only changes the fitted parameters by less than 10%. Furthermore, since GPM-DPR can only observe echoes with Ka > 18 dBZ, echoes likely contain precipitation sized particles like the ones observed by the surfaced based probes.

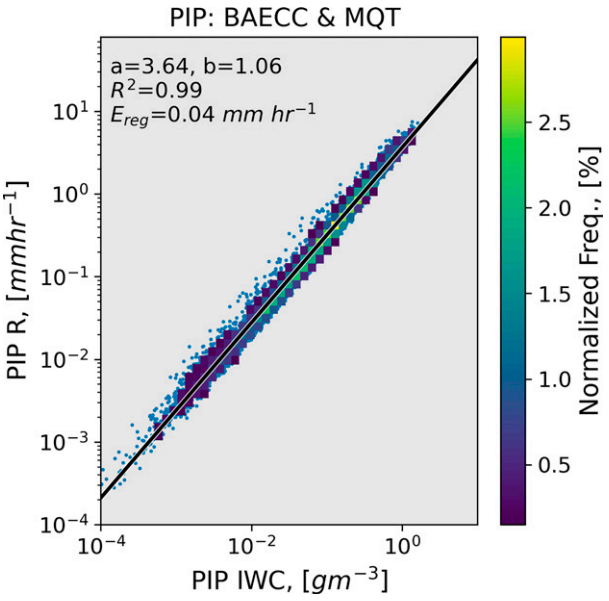

FIG. 1. Measured correspondence between IWC and liquid equivalent precipitation rate R from the datasets collected at the University of Helsinki Hyytiälä Forestry Field Station Finland (BAECC; von Lerber et al. 2017) and Marquette, Michigan (MQT; Pettersen et al. 2020). Dots indicate individual observations (5-min temporal averaging); shading shows the density of points in each bin. The black line is the power-law fit from Eq. (3), and E_{reg} is the mean error estimated from using the regression to calculate R from IWC.

b. Coincident dataset and quality control

The primary dataset used here is the coincident *CloudSat*–GPM archive (2B.CSATGPM; Turk 2016; Turk et al. 2021). This dataset consists of all GPM overpasses from April 2014 to August 2016 that have a *CloudSat* track passing through the GPM swath separated by less than 15 min in time. While any time offset can lead to errors, more strict time difference requirements (i.e., 5 min) did not change the general conclusions of this paper. The closest GPM-DPR footprint to each *CloudSat* along track footprint is deemed coincident and used for the comparison. These data have already been used successfully in informing the current status of the operational GPM-DPR retrieval of snowfall (Casella et al. 2017), determining the effectiveness of high-frequency radiometers for snowfall retrievals (Panegrossi et al. 2017, 2018; Yin and Liu

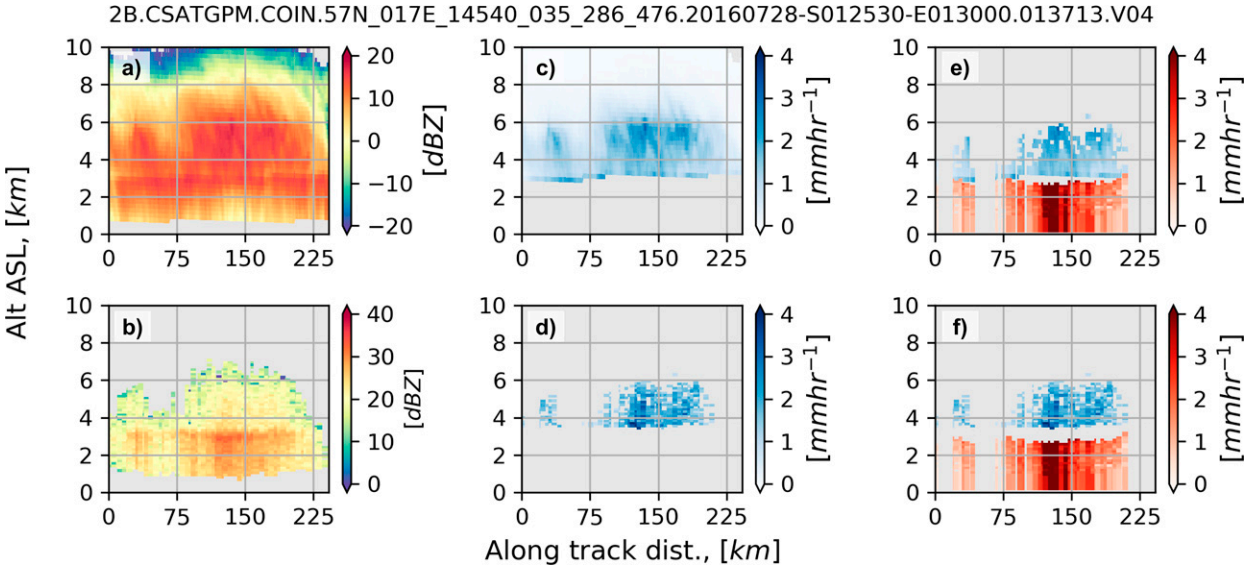

FIG. 2. An example of a coincident sample of a precipitating system located at 57°N, 145°E between 1253 and 1300 UTC 28 Jul 2016. All x axes are the along-track direction of *CloudSat*. (a) *CloudSat* W-band attenuated Z_e (dBZ) with the surface echo clutter and echo-top noise removed; (b) GPM-DPR Ka-band attenuated Z_e (dBZ) matched along the *CloudSat* track, with the surface echo clutter and echo-top noise removed. (c) 2C-SNOW-PROFILE retrieved snowfall rate (mm h^{-1}). Gates with temperatures ≥ -2.5°C and inferred mixed-phase gates (bright band) were removed. (d) Chase et al. (2021) retrieved snowfall rate (mm h^{-1}). Melting layer, rain echoes, and gates below 18 dBZ (minimum sensitivity) were removed. (e) As in (c), but now only where there is Chase et al. (2021) retrieval. The additional red colors are the default version-6 2ADPR rainfall retrieval. (f) As in (d), but with the added rainfall retrieval in red from the default version-6 2ADPR rainfall retrieval.

2019), training of passive microwave radiometers to derive snowfall properties of the column (Rysman et al. 2018) and near-surface (Rysman et al. 2019), and informing retrievals of ice water path within convective systems from passive microwave radiometers (Rysman et al. 2021).

Since the original goal of Turk (2016) was to include both coincidences of *CloudSat* with GPM-DPR, and coincidences with the much wider swath radiometer on GPM (GMI; Draper et al. 2015), there are many files with little to no meteorological signal from GPM-DPR. To remove files containing no valid GPM-DPR snowfall retrievals, a list of files was identified manually to contain GPM-DPR signal. Then from the shorter list of coincident orbits, each file was quality controlled to be used for analysis in section 3 as discussed below.

First, echoes determined as convective by the GPM-DPR retrieval (i.e., no bright band present) are removed. Convective profiles are removed because the NN retrieval is not expected to perform well in convection given the likely presence of large amounts of supercooled liquid water and riming, which are not included in the formulation of the NN retrieval (cf. Chase et al. 2021). Then surface echoes are removed by using the included surface elevation with a buffer of 1 km for the *CloudSat* dataset and the GPM-DPR supplied lowest clutter free bin parameter for the GPM-DPR dataset. Subsequently, the noise above echo top is eliminated by using the minimum sensitivity thresholds for each radar, which are −25, 18, and 12 dBZ for W, Ka, and Ku bands, respectively. The result from the aforementioned steps is shown in Figs. 2a and 2b. To isolate solid-phase echoes, the melting layer was removed by removing gates with temperatures > -2.5°C, where the temperature is obtained by the closest ECMWF auxiliary (ECMWF-AUX) profile included within the matched dataset. The threshold of −2.5°C was chosen to be conservative and to assure most of the melting layer would be excluded from the analysis. The result of removing liquid-phase echoes from the retrieved R are found in Figs. 2c and 2d. Afterward, the 2CSP retrieval is then constrained to where the NN retrieval was successfully performed (i.e., where there is Ku and Ka signal). Profiles where at least three valid gates (i.e., meet the aforementioned conditions) within the ice layer are kept for the analysis and all others are removed.

Since there is no "ground truth" of retrieved snowfall within the Turk (2016) dataset, one way to evaluate retrieval performance is to compare the liquid equivalent mass flux (i.e., R) right above the melting layer with the mass flux right below the melting layer. Heymsfield et al. (2018) used this method, suggesting that on average the mass flux above and below the melting layer should be quasi-conserved. While this may not be directly intuitive, given the fall velocity of melted particles is much faster than their solid-phase counterparts, the number concentration of particles scales inversely with the fall velocity, thus the mass flux should be quasi-conserved. Additional evidence for the quasi-balance of R across the melting layer is shown in a recent case study by Mróz et al. (2020) using triple-frequency Doppler spectra measurements. It was shown that the mass flux just above the melting layer is

well preserved just below the melting layer outside of regions of intense aggregation (e.g., where the dual-frequency ratio at X-Ka is greater than 10 dB). Last, since the retrieval of rain from radars is generally more constrained (e.g., raindrops are quasi-spherical; constant density) the rainfall retrieval, supplied from version 6 of the 2ADPR algorithm, just below the melting layer is used as a benchmark for the snowfall retrievals just above the melting layer. Thus, as a final constraint on the dataset, a rain echo with at least three gates had to be present for the profile to be used in the analysis. The final result of all the quality control is found in Figs. 2e and 2f. A separate dataset of near-surface snowfall events (i.e., 0°C isotherm below the clutter echo) is also analyzed in the same manner, but the final constraint of the rain echo requirement is removed. While there is no baseline estimate to suggest which snowfall retrieval is performing better, the near-surface snowfall analysis is included to assess if trends from the snow over rainfall persist to snow only cases. After quality control there are a total of 3657 profiles of coincident retrievals of snowfall above rain and 1322 profiles of coincident retrievals of snowfall near the surface. (A map of the location of all the profiles can be found in Fig. A1.)

c. *Field campaign data*

To supply discussion of the differences between 2CSP and the NN retrieval, two case studies using observations are shown. Specifically, a flight leg obtained as part of the Investigation of Microphysics and Precipitation for Atlantic Coast-Threatening Snowstorms (IMPACTS; McMurdie et al. 2022) and a flight leg from Olympic Mountains Experiment (OLYMPEX; Houze et al. 2017) are used. During both of the field campaigns, coordinated flights between a higher-altitude aircraft carrying radars and a lower-altitude aircraft carrying in situ probes were frequently conducted in order to obtain coincident measurements of remotely sensed variables, like Z_e, and in situ measurements. The specific radars used in this analysis are the Airborne Precipitation Radar (Sadowy et al. 2003), version 3 (APR3; Durden et al. 2019); the Cloud Radar System (CRS; Li et al. 2004); the High Altitude Imaging Wind and Rain Profiler (HIWRAP; Li et al. 2016); and the ER-2 Doppler Radar (EXRAD; Heymsfield et al. 1996).

The APR3 is a triple-frequency scanning radar measuring collocated Z_e at Ku (13.4 GHz), Ka (35.6 GHz), and W band (94 GHz), which was flown on NASA's DC-8 during the OLYMPEX field campaign. The APR3 measurements are estimated to have a calibration uncertainty of 1–1.5 dB after being calibrated to the surface echo of the ocean surface in clear conditions and comparisons of the dual-frequency ratio measured in low-Z_e regions of cloud top (Tanelli et al. 2006). The other three radars, CRS, HIWRAP, and EXRAD, are all nadir-pointing Doppler radars that measure at W (94 GHz), Ka (35.6 GHz), Ku (13.9 GHz), and X (9.6 GHz) bands. The CRS, HIWRAP, and EXRAD were flown together aboard the ER-2 aircraft for IMPACTS. Calibration of the radars was performed in a similar way as the APR3 and are estimated to have a calibration uncertainty of 1 dB. All measured frequencies of Z_e are corrected for gaseous attenuation of O_2 and H_2O using a dropsonde for OLYMPEX, a balloonborne radiosonde for IMPACTS, and the 2013 report from the Radiocommunication Sector of International Telecommunication Union 2013 implemented in pyLayers (https://github.com/pylayers/pylayers). Mean two-way attenuation correction for gaseous extinction is 0.2, 0.4, and 0.6 dB for Ku, Ka, and W band, respectively.

Simultaneous cloud in situ data were collected during both field campaigns. For OLYMPEX, in situ observations were collected on board the University of North Dakota (UND) Cessna Citation aircraft (Delene et al. 2019), while for IMPACTS they were collected on NASA's P3 aircraft. Beyond the common state parameters measured (e.g., pressure, temperature, relative humidity), the in situ aircraft carried the same optical array probes (OAP) to measure the particle size distribution within clouds. Specifically, they had a two-dimensional stereo (2DS) and a high-volume precipitation spectrometer, version 3 (HVPS3). The OAP data are quality controlled using the University of Illinois–University of Oklahoma Optical array Probe Software (UIOOPS; McFarquhar et al. 2017; Jackson et al. 2014) to correct images that are hollow, remove shattered artifacts and reconstruct particles that have dimensions larger than the OAP diode array. The 2DS and HVPS data are combined to give size distributions between 175 μm and 3 cm, with a transition between the probes at 1 mm. Particles smaller than 175 μm are not included because of a small and uncertain depth of field, and such small particles do not contribute significantly to calculated IWC.

Unfortunately, for the case from IMPACTS there was not good collocation between the radar carrying aircraft and the in situ aircraft. Thus, to provide additional support for the hypotheses discussed in this paper the following three additional datasets are included in the discussion in section 3b. The first one is the Multi-Radar Multi-Sensor (MRMS) radar only precipitation rate retrieval (Zhang et al. 2011). While the MRMS radar only precipitation rate is a static power-law between Z_e and R (i.e., a single Z–R relationship), it has been used before in evaluating various snowfall retrievals from space in the United States (Cao et al. 2014; Mróz et al. 2021). The second dataset is surfaced-based measurements of R from three nearby stations. One of the three stations is a standard Automated Surface/Weather Observing Systems (ASOS) station located at the Syracuse, New York, airport. The other two stations are a part of the New York State Mesonet (Brotzge et al. 2020).

3. Results and discussion

a. *Coincident statistics between GPM-DPR and CPR*

Statistics of measured and retrieved variables from all coincident measurements between CPR and GPM-DPR after quality control are shown in Fig. 3. For surface rainfall events, the median profile of measured Z_e for GPM-DPR generally increases with temperature, from 19.7 and 21.6 dBZ to 21.5 and 25.6 dBZ for Ka and Ku band, respectively (red and blue lines; Fig. 3a). Meanwhile, the CPR median measured Z_e

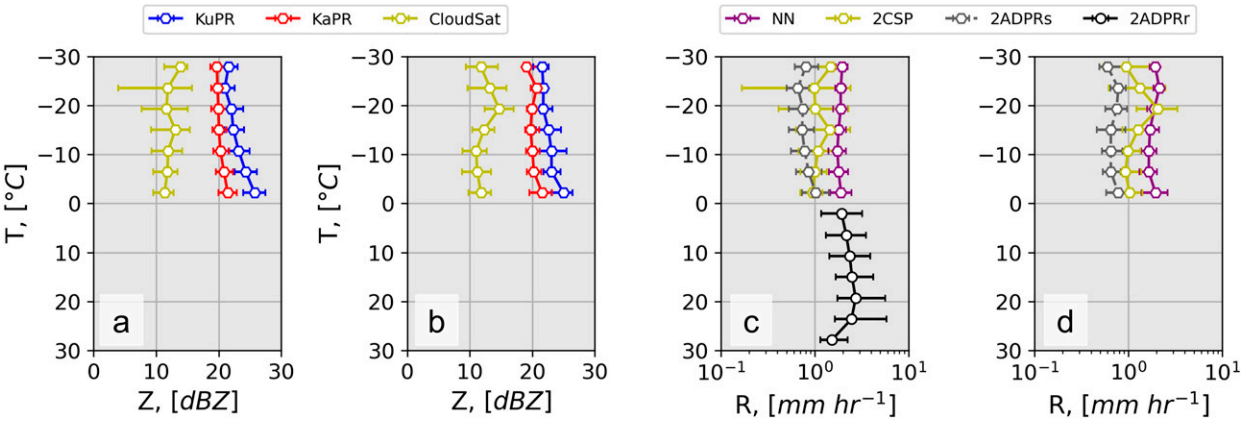

FIG. 3. Statistics of measured and retrieved variables for all coincident orbits within which precipitation was detected by GPM-DPR Ka-band radar (see the appendix for a map of these locations). (a) Median profiles (line with symbols) of measured Z_e from *CloudSat* (dBZ; yellow), GPM-DPR Ka band (red), and GPM-DPR Ku band (blue) for (a) surface rain events and (b) near-surface snowfall events. The horizontal lines with caps are the locations of the 25th and 75th quantile. Medians and quantiles were calculated in linear units and then converted to logarithmic units. (c) As in (a), but for median profiles (line with symbols) of the retrieved snowfall rate (mm h^{-1}; hexagon symbols) adjusted to mean sea level pressure (1013 hPa) from 2CSP (yellow), NN (purple), and version 6 of 2ADPR (gray) for all stratiform instances with snow measured above rain. Version 6 of the 2ADPR rainfall retrieval is in black with circles. (d) As in (c), but for instances in which the 0°C isotherm was found below the lowest clutter free gate (i.e., near-surface snow events).

decreases from 13.8 to 11.4 dBZ (yellow line; Fig. 3a). As a first-order approximation, the retrieval of R just below the melting layer is compared with the retrieval of R just above the melting layer. Heymsfield et al. (2018) and Mróz et al. (2020) suggested that R should be approximately conserved through the melting layer. Thus, if the assumptions of mass flux conservation are true on average, which implies relative humidity with respect to water (RH) is near 100%, then R is approximately conserved. Note that Heymsfield et al. (2018) show that a modest decrease in RH (95%) can result in a non-negligible reduction in R across the melting layer (23%; cf. Fig. 1 in Heymsfield et al. 2018), but if the RH is indeed less than 100% on average for the profiles studied here, then the rain retrieved R would be a lower bound to the snowfall retrieved R. In Fig. 3c the NN retrieval is closest to the rainfall retrieval, with a median value of 1.9 mm h^{-1} and a percent difference from the rain retrieval of +2%. The next closest to the rain retrieval is the 2ADPR snowfall retrieval and then 2CSP, with median values of 1.01 and 0.95 mm h^{-1} and percent differences with respect to the rain retrieval of −48% and −51%, respectively. Considering the profiles over all temperatures, the smallest values of R in the snow layer are retrieved from 2ADPR, followed by the 2CSP and then the NN retrieval. The slopes of retrieved R for 2ADPR and 2CSP generally follow the shapes of the reflectivity that make up their retrieval (Fig. 3a; while the NN retrieval is effectively constant for all temperatures, but does show an increase from 1.74 mm h^{-1} at −10°C to 1.9 mm h^{-1} at −2.5°C. Events where there is no rain retrieval available to be used as a reference (i.e., 0°C in or at lower altitudes than the ground clutter) are shown in Figs. 3b and 3d. The pattern overall is the same as the profiles with a coincident rain retrieval (Figs. 3a,c). The smallest retrieved R is produced by the 2ADPR algorithm followed by the 2CSP and the NN retrieval, respectively.

While the comparison with the GPM-DPR rainfall retrieval was informative for gates near 0°C, unfortunately there are no reference data with which to compare the three snowfall retrievals at temperatures lower than −2.5°C. Thus, it is impossible to provide an objective assessment of which retrieval is performing best at lower temperatures. Although, given there are measurements of reflectivity at Ku, Ka, and W bands, some hypotheses can be postulated. The general increase of Z_e at Ku and Ka bands, paired with a general decrease of W band, suggests a few possible scenarios that could result in the decrease of Z_e and subsequently a decrease of 2CSP R from −15° to −2.5°C:

1) the diminished Z_e is due to attenuation and the 2CSP algorithm does not adequately compensate for it,
2) the diminished Z_e is due to non-Rayleigh scattering and the actual scattering is inconsistent with 2CSP's non-Rayleigh scattering property assumptions, and/or
3) the diminished Z_e is influenced by multiple scattering that is inconsistent with 2CSP's multiple-scattering treatment.

These three potential explanations are not mutually exclusive nor are they an exhaustive list of everything that may be occurring. Furthermore, all the listed processes could be affecting the observed Z_e and the 2CSP retrieval to some extent even though the 2CSP algorithm does attempt to account for these effects.

For scenario 1, the observed W-band Z_e at temperatures of −15°C and warmer are large for *CloudSat* CPR observations, exceeding 10 dBZ, but are diminished relative to the Ku- and Ka-band Z_e. This suggest large ice water contents that, for W band, are likely to produce substantial attenuation. Although the 2CSP retrieval algorithm is designed to compensate for attenuation, two factors come into play. First, when the observed Z_e and associated attenuation become large, the

retrieval's forward model becomes more uncertain. This causes the retrieval to rely more on a priori assumptions about particle size distributions. These a priori assumptions may not be consistent with the observed conditions and lead to an error in the retrieved R. Under these conditions, the retrieved R has large uncertainty. Second, the conditions of −15°C and warmer are likely to contain supercooled water and rimed particles (Kneifel and Moisseev 2020), which may lead to large particle densities and stronger attenuation at W band relative to the aggregate-like particle model used in the 2CSP retrieval. Considering only the attenuation effects, if the 2CSP particle models produce too little attenuation, the retrieval algorithm's estimate of the unattenuated Z_e will be too small and will lead to R being underestimated.

For scenario 2, larger snow particles observed at shorter wavelengths (e.g., Ka and W band) have non-Rayleigh scattering properties that vary depending on the assumed particle type (e.g., Kneifel et al. 2011; Tyynelä et al. 2011; Leinonen and Szyrmer 2015). The diminished Z_e observed by *CloudSat* (Figs. 3a,b) coincides with warmer temperatures, which are more likely to contain larger particles (i.e., aggregates Hobbs et al. 1974), and there is an increased likelihood of non-Rayleigh scattering than there is with colder temperatures. Since there is considerable uncertainty in the backscatter cross sections for these non-Rayleigh scattering particles (e.g., dendrite vs bullet rosette; Wood et al. 2015), the 2CSP's assumed particle type could be misestimating the backscattering cross-section. If the cross sections are overestimated, this in turn would lead to R being underestimated. Given that the scattering regime (Rayleigh vs non-Rayleigh) of a particle is mainly determined by its size relative to the wavelength of the radar, the W-band observations of *CloudSat* would be more affected by non-Rayleigh scattering than would the Ku- or Ka-band observations of the DPR.

For scenario 3, for the conditions being discussed (large particles and large water contents), multiple scattering is important for *CloudSat*. Matrosov and Battaglia (2009) found that multiple scattering in heavier snowfall events increases the observed Z_e and partially offsets the effects of attenuation. They show that on average the amount of total extinction (the combined effects of attenuation and multiple scattering) is a net reduction of 1–2 dB in the observed reflectivity. For stratiform precipitation the 2CSP retrieval similarly assumes that multiple scattering partially offsets the amount of attenuation but treats this as a significant forward-model uncertainty (Wood and L'Ecuyer 2018). Matrosov and Battaglia (2009) used spheroidal particles and the T-matrix approach to simulate the snow particle scattering properties, and spheroidal particles have been shown to be less accurate models when compared with more physically realistic shapes modeled using the discrete dipole approximation (Tyynelä et al. 2011; Kneifel et al. 2011). The impacts that more accurate particle models would have on the balance between attenuation and multiple scattering are not known. If the 2CSP retrieval overestimates the compensating effect of multiple scattering, the result would be an underestimate of R. To fully assess the impacts of multiple scattering and attenuation, new Monte Carlo simulations [i.e., like the ones done in Matrosov and Battaglia (2009)] with more realistic particle shapes and rime fraction are required, which is beyond the scope of this paper.

b. *Case studies*

In this section, two case studies from NASA field campaigns assist in providing additional discussion on scenarios where W-band radar shows decreasing Z_e while Ku and Ka bands show increasing Z_e at larger temperatures. Each case study was specifically chosen to exemplify potential analog samples from Fig. 3, but with much higher resolution and better sensitivity radar systems. Furthermore, both case studies provide some external in situ observations as a reference for the different snowfall retrievals.

1) IMPACTS: 1508 UTC 7 FEBRUARY 2020

The first case study examined is from IMPACTS. This case is analogous to the profiles measured in Figs. 3b and 3d (i.e., surface snowfall events). On 7 February 2020, a deepening midlatitude cyclone was moving eastward across Pennsylvania, producing a large precipitation shield over central New York (Fig. 4). Snowfall accumulation at the surface for this event exceeded 233 mm (liquid equivalent 35 mm) at Syracuse. The IMPACTS field campaign targeted the north side of the cyclone, where they flew a racetrack pattern from Syracuse to Albany, New York, and back. Data from one of the three coincident flight legs between both aircraft are shown in Fig. 5.

The cross sections of measured Z_e at W band (Fig. 5a) and Ku band (Fig. 5b) show different perspectives of the same cyclone. Median W-band Z_e grows to maximum 16.9 dBZ near 4 km and then reduces to 7.8 dBZ at 0.5 km (yellow; Fig. 5e). Meanwhile, X-, Ku-, and Ka-band reflectivity are at a maximum near 1.5 km with values of 29.5, 28.7, and 23.8 dBZ, respectively (black, blue, and red lines; Fig. 5e). Retrieved R from an optimal estimation retrieval using the exact assumptions as the 2CSP retrieval is shown in Fig. 5c, while the NN retrieved R is shown in Fig. 5d. As expected, both R retrievals generally follow the Z_e used within each respective retrieval. The two separate retrievals are relatively close in magnitude from 8 to 6 km, but then deviate from 6 km toward the surface. The 2CSP-like retrieval shows a peak in median R near 5 km with a value of 1.88 mm h^{-1}, then decreases to a value of 1.5 mm h^{-1} at 4 km (yellow line; Fig. 5f), and then increases to about 2 mm h^{-1} at 0.5 km. Meanwhile the NN retrieved R increases with decreasing altitude, peaks around 2.5 km with a value of 2.93 mm h^{-1} (purple line; Fig. 5f) and then reduces to 2.81 mm h^{-1} a 0.5 km. Unfortunately, during this cross section the in situ aircraft was turning into the ER-2 flight track after the ER-2 already sampled the region. Thus, the in situ data are not matched well and could not be used for evaluation of the retrievals.

As an alternative evaluation method, the MRMS-retrieved R and the measured R from three surfaced based gauges nearby the flight track are analyzed in Figs. 5f and 6. The median MRMS-retrieved R over the distance of the flight track is 2.8 mm h^{-1}, which is effectively the same as the NN retrieval. Meanwhile the minimum measured MRMS-retrieved R along

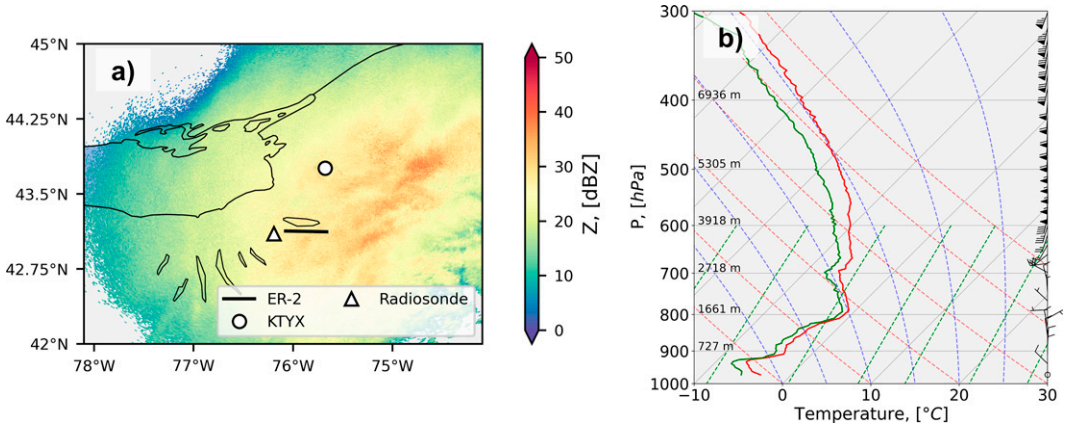

FIG. 4. Map and sounding from a case study from the IMPACTS field campaign from 1508:25 to 1510:50 UTC 7 Feb 2020. (a) The radar scan is from the lowest elevation (0.5°) from the KTYX NEXRAD radar (circle) at 1507 UTC. The black line is the ground track of the airborne radars. The triangle is where a ground-based radiosonde was launched at 1414 UTC. (b) Skew T diagram of the radiosonde. Wind barbs are in knots (1 kt ≈ 0.5 m s^{-1}).

the flight track is 2.0 mm h^{-1} (black circle; Fig. 5f), which is closest to the 2CSP median retrieved value. The surface-based gauges at the time of the radar overpass (1509 UTC) show R ranging from 1.5 mm h^{-1} at Syracuse to 5.16 mm h^{-1} measured at Westmoreland, New York. Since tipping-bucket gauges (Syracuse is a tipping-bucket gauge) can have issues with measuring snowfall rates (e.g., Rasmussen et al. 2012), there is more confidence with the Fayetteville (New York) and Westmoreland stations, which are Pluvio2 weighing bucket gauges in a fenced enclosure (Brotzge et al. 2020). Thus, all radar-retrieved R are low biased at the time of the flight relative to Fayetteville, with percent differences of 127%, 63%, and 62% for the 2CSP, MRMS, and NN retrieval, respectively.

While the aforementioned analysis is just one case study, given the results of the statistical comparison of section 3a and this section in combination, there is empirical support showing that the 2CSP retrieval of R could be low biased in

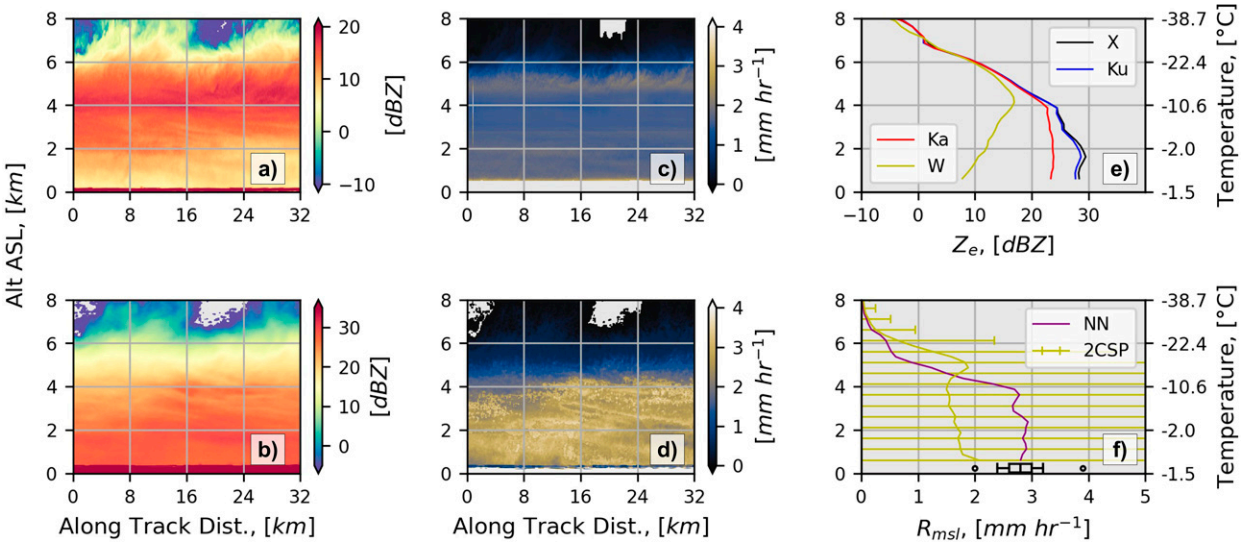

FIG. 5. A case study from the IMPACTS field campaign from 1508:25 to 1510:50 UTC 7 Feb 2020. (a) Nadir W-band and (b) Ku-band Z_e (dBZ) corrected for gaseous attenuation of O_2 and H_2O. (c) Retrieval of R from the W-band-only *CloudSat*-like retrieval (mm h^{-1}). (d) Calculation of R from the NN retrieval of D_m and N_w (mm h^{-1}). (e) Median profiles of X (black), Ku (blue), Ka (red), and W band (yellow) along the cross section. The tick labels on the right are approximate temperatures for each height inferred from radiosonde measurements. (f) As in (e), but now showing the median R from the *CloudSat*-like retrieval (2CSP; yellow) and the NN retrieval (purple). The error bars on the 2CSP median are the median uncertainty estimated from the optimal estimation retrieval. The black boxplot located at 0.5 km is the 0th, 10th, 25th, 50th, 75th, 90th, and 100th percentile of MRMS-retrieved R along the flight track.

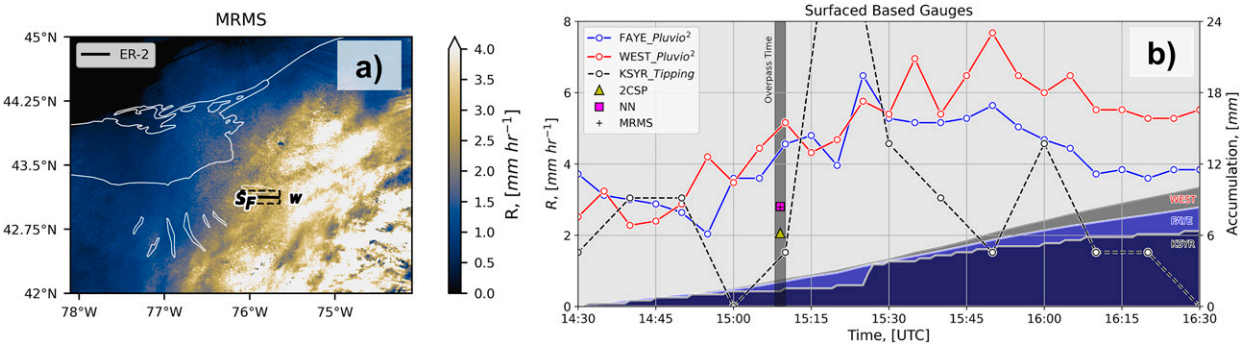

FIG. 6. Additional snowfall measurements for 7 Feb 2020. (a) Mean MRMS-retrieved precipitation rate from 1506 to 1508 UTC for the same location as Fig. 4a. Letters S, F, and W correspond to the named surface stations Syracuse, Fayetteville, and Westmoreland, respectively. The black solid line is the flight track in Fig. 5, and the dashed black-outlined rectangle is the area over which the MRMS data are tabulated for the statistics in (b). (b) Time series of the surfaced based gauges in (a). The left *y* axis corresponds to the lines, and the right axis corresponds to the filled curves. The data for Syracuse, Fayetteville, and Westmoreland are in black, blue, and red, respectively. The median retrieved value from Fig. 5f is also shown at 1509 UTC for 2CSP (yellow triangle), the NN (purple square), and MRMS (black plus sign).

moderate to intense (Ka > 18 dBZ) snowfall events. This case study also shows that the NN retrieval and the retrieval from MRMS could also be low biased relative to surface-based gauges. Future field campaigns, such as IMPACTS year 2–3, should aim to collect more cases to help to characterize these events by designing flight tracks to coincide directly with surface-based measurements of snowfall and have better collocation with an in situ aircraft.

2) OLYMPEX: 0646 UTC 18 DECEMBER 2015

The second case study examined is from OLYMPEX. This case is analogous to the profiles measured in Figs. 3a and 3c (i.e., surface rainfall events). On 18 December 2015, an occluded front was moving eastward from the Pacific Ocean toward the Olympic Peninsula in Washington State forcing widespread stratiform precipitation (Fig. 7). The OLYMPEX field campaign conducted three coincident flights between the NASA's DC-8 and the UND Citation over the same east–west track. One of the coincident flights from over the ocean is shown in Fig. 8.

As opposed to the previous case in which surface snowfall was observed, Fig. 8b shows a clear melting level (i.e., bright band) located at 1.6 km that highlights the phase transition from snow to rain. Thus, this case provides a potential example of the cases shown in Figs. 3a and 3c and closely resembles the structure in Fig. 2. As in the previous case, the W-band Z_e (Fig. 8a) and Ku-band Z_e (Fig. 8b) show different vertical variations for the same precipitation. W-band Z_e increases to a maximum at 4.1 km of 12.7 dBZ and then fluctuates down and back up to 12.7 dBZ at 2.9 km. From 2.9 km, the W-band Z_e decreases to 9.1 dBZ at 1.9 km (Fig. 8e). The other

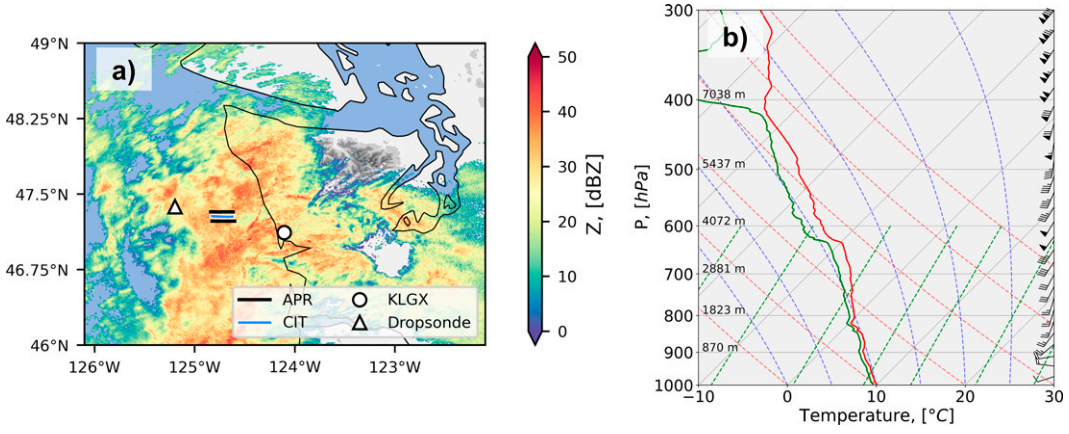

FIG. 7. As in Fig. 4, but for a case study from the OLYMPEX field campaign from 0647:48 to 0649:17 UTC 18 Dec 2015. (a) The ground-based radar used is the KLGX radar from 0649 UTC. The black lines are the extent of the APR3 swath, and the blue line is the in situ aircraft. The triangle is a dropsonde, dropped from the APR3 aircraft at 0557 UTC. (b) Skew *T* diagram of the dropsonde data in (a).

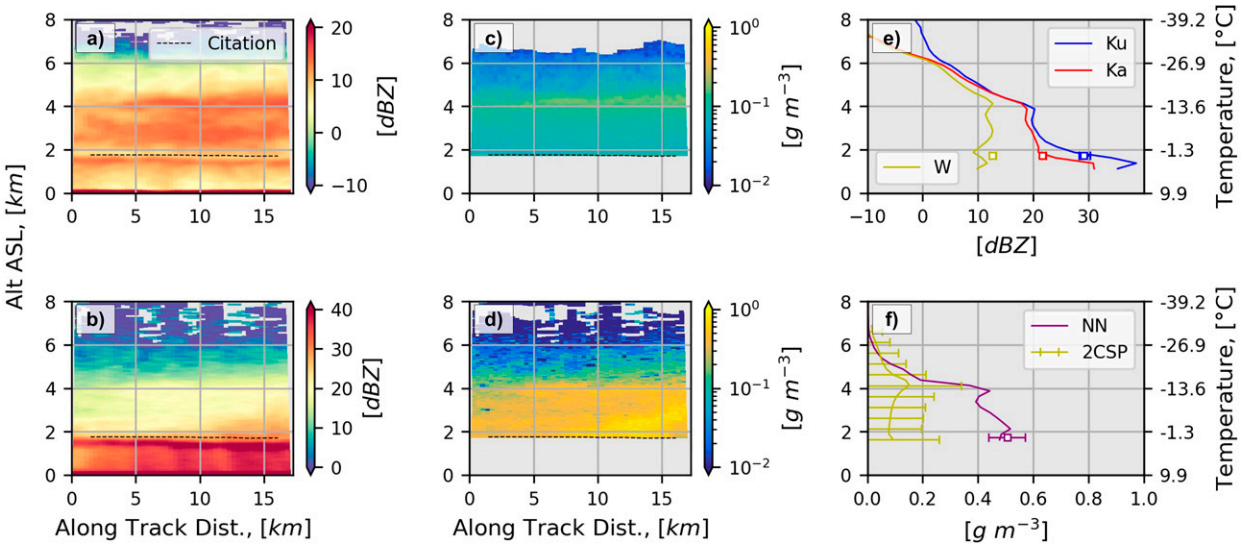

FIG. 8. Similar to Fig. 5, but for a case study from the OLYMPEX field campaign from 0647:48 to 0649:17 UTC 18 Dec 2015 and now the retrieved parameter from the radars is (c),(d),(f) ice water content. Furthermore, (e) and (f) now have symbols with caps that indicate the 25th, 50th, and 75th percentiles calculated from the in situ measured PSD using Leinonen and Szyrmer (2015) backscatter cross sections.

measured frequencies show increasing Z_e throughout most of the profile, reaching a maximum before melting of 20.9 and 27.4 dBZ for Ka and Ku band, respectively (Fig. 8e). Here, IWC is compared because there are fewer assumptions in the measurement of IWC from the in situ aircraft. The retrieved IWC follows the general shape of the measured Z_e used in the respective retrievals (Figs. 8c,d). The 2CSP retrieval suggests a maximum IWC of 0.15 g m^{-3} at 4.1 km and then decreases to 0.08 g m^{-3} at 2 km (Fig. 8f). Meanwhile, the NN retrieved IWC agrees with the 2CSP routine from 8 km to around 4 km but then is approximately 6 times as large at 2 km, with the maximum IWC of 0.51 g m^{-3} (Fig. 8f).

For this case, the in situ aircraft was flying at an average altitude of 1.7 km (−0.5°C), right within the observed reduction of W-band Z_e. This location of reduced Z_e at W band has been termed the radar "dark" or "dim" band in the literature (e.g., Sassen et al. 2005; Heymsfield et al. 2008; Kollias and Albrecht 2005; Sassen et al. 2007). The IWC calculated from the measured particle size distribution by assuming moderately rimed aggregates from Leinonen and Szyrmer (2015) ($\alpha = 0.249$ kg m$^{-\beta}$; $\beta = 2.30$ for the mass–dimension relation) shows the best agreement with the measured Ku- and Ka-band reflectivity (symbols with error bars; Fig. 8e) and suggests median IWC values close to the NN retrieved IWC of 0.51 g m^{-3}. Thus, it is expected that the NN retrieval is more plausible given that the 2CSP retrieval of IWC is smaller by a factor of 6 than the in situ data and that the in situ data can reproduce the measured median Z_e to within 2 dB.

Figure 9 shows the measured particle size distribution and some particle images from the in situ aircraft. Large aggregates with dimensions exceeding 1 cm are observed, with particles greater than 2 cm observed near the end of the flight. Using the Cloud Droplet Probe and the Rosemount Icing Detector, there is limited or no supercooled liquid water present in the sampled layer (not shown). On average, larger mean particle sizes results in larger Z_e (cf. Fig. 4 in Kneifel et al. 2011). Since Ku- and Ka-band Z_e increase across this layer, and melting is not detected by the in situ instruments (e.g., temperature less than 0°C, images are nonspherical, low CDP measurements) mean particle size should be increasing. Thus, the measured reduction in Z_e at W band can only be explained by non-Rayleigh scattering effects and/or attenuation. Although there is no method to disentangle the attenuation and non-Rayleigh effects, it is clear that the radar-measured Z_e, which is ultimately used in the retrievals, is low relative to the PSD calculated Z_e (yellow symbol and yellow line in Fig. 8e), resulting in a smaller retrieved IWC at the level of in situ observations.

4. Conclusions

With the advent of spaceborne radars, the global estimation of precipitation and the quantification of the hydrologic cycle has been enhanced. Both CPR and GPM-DPR provide unique opportunities to study snowfall near the surface and snow properties throughout the atmospheric column. For the first time, a direct quantitative comparison of the 2C-SNOW-PROFILE (2CSP; Wood and L'Ecuyer 2018, 2021), 2ADPR (Iguchi et al. 2018), and a neural network retrieval (Chase et al. 2021) on coincident measurements globally was conducted. The main conclusions from the comparison of over 3500 precipitating profiles are as follows:

1) The neural network snowfall retrieval just above the melting layer from Chase et al. (2021) provided the best agreement to the rain layer retrieved precipitation rate R from 2ADPR just below the melting layer.

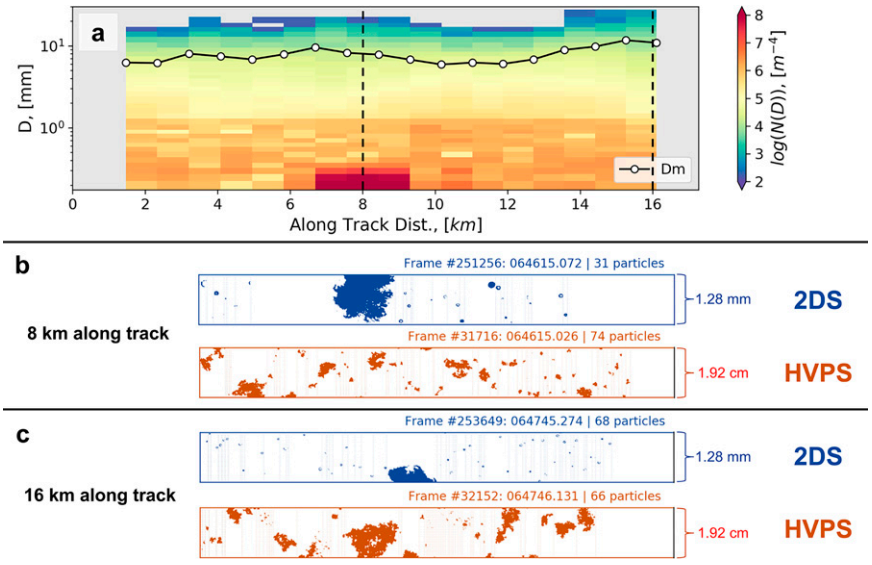

FIG. 9. In situ observations from 18 Dec 2015. The in situ aircraft is located by the dashed line in Fig. 8. (a) Measured $N(D)$ with the same x scale as Fig. 8 (shading). The line with symbols is the mass-weighted mean diameter assuming the same m–D from Leinonen and Szyrmer (2015) that recreates the measured Z_e in Fig. 8. Also shown are example particle images from both the 2DS (blue) and the HVPS (orange) from the (b) 8- and (c) 16-km locations on the x axis.

2) *CloudSat*'s 2CSP retrieval showed decreasing R with temperatures greater than −15°C, decreasing by about 35% in magnitude from −15° to −2.5°C and underestimating relative to the rain layer retrieved R from GPM-DPR.
3) GPM-DPR's 2ADPR snowfall retrievals for most temperatures showed the smallest retrieved R in comparison with the 2CSP and the NN retrieval.

It should be emphasized that the data that resulted in the conclusions above are from profiles that have at least three gates of 18 dBZ Ka-band Z_e within the ice layer. Thus, the profiles used in the analysis are likely in the upper tail of the distribution of intensity for stratiform precipitation, but it is expected that while these profiles are less frequent in terms of total number, they likely have a disproportionate effect on the total accumulation of precipitation. Initial investigations have shown the GPM-DPR is not well suited for capturing the entire distribution of snowfall accumulation (Casella et al. 2017; Skofronick-Jackson et al. 2019), but if the bias in the retrieved R from 2CSP reported in Fig. 3 also exists at lower temperatures and occurs within a large fraction of snowfall events within the *CloudSat* record, then there is opportunity for GPM-DPR to assist in the quantification of the moderate to intense snowfall events since the 2CSP retrieval is highly uncertain and likely biased low. Furthermore, for the profiles used in Fig. 3 some of the assumptions made in the 2CSP optimal estimation retrieval, such as the particle model or the quasi-balance between multiple scattering and attenuation, could be inappropriate and might be what is leading to the reduction in R from −15° to −2.5°C. Future work should investigate how including new state-of-the-art particle scattering models (e.g., Kuo et al. 2016; Eriksson et al. 2018) impact the 2CSP retrieval and the expected multiple scattering with *CloudSat* geometries within moderate to intense snowfall events.

In addition to the results from the coincident GPM-*CloudSat* dataset, two case studies from NASA field campaigns highlight the apparent challenges of W band only retrievals of snowfall. The main conclusion from the two case studies is as follows: Coincident W-, Ka-, and Ku-band measurements suggest that W-band-only retrievals of IWC and R, are nonnegligibly affected by attenuation and non-Rayleigh scattering. While the overall amount of attenuation might initially seem small, 2–3 dB, its effect on the 2CSP retrieval is clearly not negligible. In both cases, the 2CSP retrieval peaks near the dendritic growth zone (−15°C) and then decreases toward greater temperatures. The analysis of the multifrequency radar measurements here further support the already documented notion that multifrequency radar measurements improve snowfall retrievals (e.g., Kneifel et al. 2011, 2015; Grecu et al. 2018; Leinonen et al. 2018; Tridon et al. 2019; Battaglia et al. 2020). Thus, it is advantageous for any future planned spaceborne missions, such as the planned international mission named the Atmospheric Observing System (AOS; https://aos.gsfc.nasa.gov), to include a longer wavelength radar (e.g., a Ka- or Ku-band system) in tandem with the W band in order to improve precipitation science and the associated scientific outcomes. The added longer wavelength will provide valuable insight to when there is appreciable attenuation/non-Rayleigh scattering at W band and hopefully inform the retrieval to rely on the longer wavelength in said regions.

Additional future work should explore the *CloudSat* record and consider the documented reduction in R with larger temperatures from this paper. For example, many studies (Liu

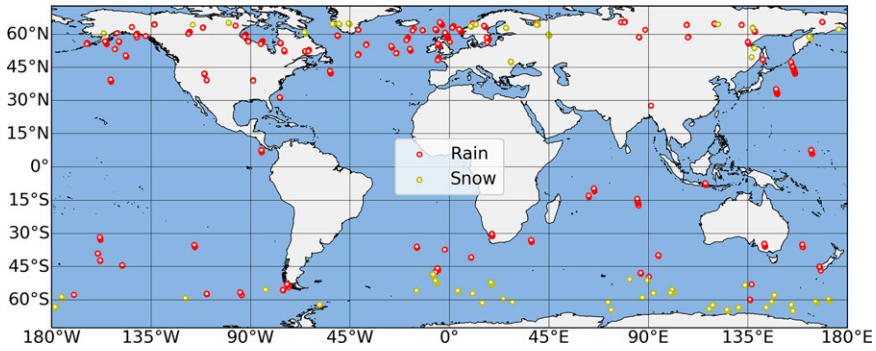

FIG. A1. Map of all footprints used in the comparison between the retrieval products.

2009; Kulie and Bennartz 2009; Palerme et al. 2014; Kulie et al. 2016; Palerme et al. 2017; Milani et al. 2018; Kulie and Milani 2018; Skofronick-Jackson et al. 2019; Cabaj et al. 2020; Edel et al. 2020; Kulie et al. 2020) have adopted the near-surface gate as the source of data to analyze when calculating the distribution of global snowfall accumulation and its properties. Rather, the entire profile of measured Z_e should be considered in order to diagnose when unexpected reductions in W-band Z_e could be occurring, and thus the frequency and effect of these attenuated profiles on the global snowfall accumulation could be estimated. While stratiform profiles were mainly used in this paper, shallow convective clouds that make up a nonnegligible fraction of total snowfall over the ocean (Kulie et al. 2016) also have considerable attenuation issues at W band (Battaglia and Panegrossi 2020) and should be carefully considered as well. Finally, other future work should update the analysis presented here with the extended coincident dataset after August 2016, when the required products from *CloudSat* are available.

Acknowledgments. This paper is dedicated to Dr. Gail Skofronick-Jackson who funded this research and provided constant support to precipitation research. More specifically, the funding for this research was provided to the University of Illinois by NASA Precipitation Measurement Missions Grant 80NSSC19K0713, NASA Earth System Science Fellowship 80NSSC17K0439, and NASA IMPACTS Grant 80NSSC19K0399 awarded to the University of Oklahoma. Work by author Wood was performed at the University of Wisconsin–Madison for the Jet Propulsion Laboratory, California Institute of Technology, sponsored by the National Aeronautics and Space Administration and under NASA Precipitation Measurement Missions Grant 80NSSC19K0732. We thank all of the participants of OLYMPEX and IMPACTS for collecting the data used in this study. We also thank Joe Turk for his work and effort to supply the coincidence dataset between GPM and *CloudSat*. Last, we thank the two anonymous reviewers and Dr. Alain Protat for their constructive comments during the review process.

Data availability statement. The coincident dataset between *CloudSat* and GPM-DPR can be found on NASA GPM's arthurhou ftps on each of their respective days after free registration with NASA's PPS (register here: https://registration.pps.eosdis.nasa.gov/registration/). For example, you can find a file at this address: https://arthurhouhttps.pps.eosdis.nasa.gov/gpmdata/2014/05/05/radar/2B.CSATGPM.COIN.64S_157W_04420_000_250_866.20140505-S011851-E012159.001032.V04.nc4. Within the coincident files are the 2CSP retrievals and the matched reanalysis data. To retrieve the GPM-DPR 2ADPR data, the 2ADPR files need to be downloaded from the same ftps location (https://doi.org/10.5067/GPM/DPR/GPM/2A/05). The neural network retrieval from Chase et al. (2021) can be found online (https://doi.org/10.13012/B2IDB-0791318_V2). The IMPACTS (https://doi.org/10.5067/IMPACTS/DATA101) and the OLYMPEX (https://doi.org/10.5067/GPMGV/OLYMPEX/DATA101) data can be found on the GHRC.

APPENDIX

Map of Profile Locations

Figure A1 is a map of all of the profiles used in Fig. 3.

REFERENCES

Adhikari, A., and C. Liu, 2019: Geographical distribution of thundersnow events and their properties From GPMKu-band radar. *J. Geophys. Res. Atmos.*, **124**, 2031–2048, https://doi.org/10.1029/2018JD028839.

——, ——, and M. S. Kulie, 2018: Global distribution of snow precipitation features and their properties from 3 years of GPM observations. *J. Climate*, **31**, 3731–3754, https://doi.org/10.1175/JCLI-D-17-0012.1.

Battaglia, A., and G. Panegrossi, 2020: What can we learn from the *CloudSat* radiometric mode observations of snowfall over the ice-free ocean? *Remote Sens.*, **12**, 3285, https://doi.org/10.3390/rs12203285.

——, and Coauthors, 2020: Spaceborne cloud and precipitation radars: Status, challenges, and ways forward. *Rev. Geophys.*, **28**, e2019RG000686, https://doi.org/10.1029/2019RG000686.

Brandes, E. A., K. Ikeda, G. Thompson, and M. Schönhuber, 2008: Aggregate terminal velocity/temperature relations. *J. Appl. Meteor. Climatol.*, **47**, 2729–2736, https://doi.org/10.1175/2008JAMC1869.1.

Brotzge, J. A., and Coauthors, 2020: A technical overview of the New York State Mesonet standard network. *J. Atmos. Oceanic Technol.*, **37**, 1827–1845, https://doi.org/10.1175/JTECH-D-19-0220.1.

Cabaj, A., P. Kushner, C. Fletcher, S. Howell, and A. Petty, 2020: Constraining reanalysis snowfall over the Arctic Ocean using *CloudSat* observations. *Geophys. Res. Lett.*, **47**, e2019GL086426, https://doi.org/10.1029/2019GL086426.

Cao, Q., Y. Hong, S. Chen, J. J. Gourley, J. Zhang, and P. E. Kirstetter, 2014: Snowfall detectability of NASA's *CloudSat*: The first cross-investigation of its 2C-snow-profile product and National Multi-Sensor Mosaic QPE (NMQ) snowfall data. *Prog. Electromagn. Res.*, **148**, 55–61, https://doi.org/10.2528/PIER14030405.

Casella, D., G. Panegrossi, P. Sanò, A. C. Marra, S. Dietrich, B. T. Johnson, and M. S. Kulie, 2017: Evaluation of the GPM-DPR snowfall detection capability: Comparison with *CloudSat*-CPR. *Atmos. Res.*, **197**, 64–75, https://doi.org/10.1016/j.atmosres.2017.06.018.

Chase, R. J., S. W. Nesbitt, and G. M. McFarquhar, 2020: Evaluation of the microphysical assumptions within GPM-DPR using ground-based observations of rain and snow. *Atmosphere*, **11**, 619, https://doi.org/10.3390/atmos11060619.

——, ——, and ——, 2021: A dual-frequency radar retrieval of two parameters of the snowfall particle size distribution using a neural network. *J. Appl. Meteor. Climatol.*, **60**, 341–359, https://doi.org/10.1175/JAMC-D-20-0177.1.

Chen, S., and Coauthors, 2016: Comparison of snowfall estimates from the NASA *CloudSat* cloud profiling radar and NOAA/NSSL Multi-Radar Multi-Sensor system. *J. Hydrol.*, **541**, 862–872, https://doi.org/10.1016/j.jhydrol.2016.07.047.

Delanoë, J. M., A. J. Heymsfield, A. Protat, A. Bansemer, and R. J. Hogan, 2014: Normalized particle size distribution for remote sensing application. *J. Geophys. Res. Atmos.*, **119**, 4204–4227, https://doi.org/10.1002/2013JD020700.

Delene, D., K. Hibert, M. Poellot, and N. Brackin, 2019: The North Dakota Citation Research Aircraft Measurement Platform. SAE Tech. Paper 2019-01-1990, 13 pp., https://doi.org/10.4271/2019-01-1990.

Draper, D. W., D. A. Newell, F. J. Wentz, S. Krimchansky, and G. M. Skofronick-Jackson, 2015: The Global Precipitation Measurement (GPM) Microwave Imager (GMI): Instrument overview and early on-orbit performance. *IEEE J. Sel. Top. Appl. Earth Obs. Remote Sens.*, **8**, 3452–3462, https://doi.org/10.1109/JSTARS.2015.2403303.

Durden, S. L., S. Tanelli, and O. O. Sy, 2019: Comparison of GPM DPR and airborne radar observations in OLYMPEX. *IEEE Geosci. Remote Sens. Lett.*, **17**, 1707–1711, https://doi.org/10.1109/LGRS.2019.2952287.

Edel, L., C. Claud, C. Genthon, C. Palerme, N. Wood, T. L'Ecuyer, and D. Bromwich, 2020: Arctic snowfall from *CloudSat* observations and reanalyses. *J. Climate*, **33**, 2093–2109, https://doi.org/10.1175/JCLI-D-19-0105.1.

Eriksson, P., R. Ekelund, J. Mendrok, M. Brath, O. Lemke, and S. A. Buehler, 2018: A general database of hydrometeor single scattering properties at microwave and sub-millimetre wavelengths. *Earth Syst. Sci. Data*, **10**, 1301–1326, https://doi.org/10.5194/essd-10-1301-2018.

Field, P. R., and A. J. Heymsfield, 2015: Importance of snow to global precipitation. *Geophys. Res. Lett.*, **42**, 9512–9520, https://doi.org/10.1002/2015GL065497.

Gatlin, P. N., W. A. Petersen, J. L. Pippitt, T. A. Berendes, D. B. Wolff, and A. Tokay, 2020: The GPM validation network and evaluation of satellite-based retrievals of the rain drop size distribution. *Atmosphere*, **11**, 1010, https://doi.org/10.3390/atmos11091010.

Grecu, M., L. Tiana, G. M. Heymsfield, A. Tokay, W. S. Olson, A. J. Heymsfield, and A. Bansemer, 2018: Nonparametric methodology to estimate precipitating ice from multiple-frequency radar reflectivity observations. *J. Appl. Meteor. Climatol.*, **57**, 2605–2622, https://doi.org/10.1175/JAMC-D-18-0036.1.

Heymsfield, A., A. Bansemer, N. B. Wood, G. Liu, S. Tanelli, O. O. Sy, M. Poellot, and C. Liu, 2018: Toward improving ice water content and snow-rate retrievals from Radars. Part II: Results from three wavelength radar-collocated in-situ measurements and *CloudSat*–GPM–TRMM radar data. *J. Appl. Meteor. Climatol.*, **57**, 365–389, https://doi.org/10.1175/JAMC-D-17-0164.1.

Heymsfield, A. J., A. Bansemer, S. Matrosov, and L. Tian, 2008: The 94-GHz radar dim band: Relevance to ice cloud properties and *CloudSat*. *Geophys. Res. Lett.*, **35**, L03802, https://doi.org/10.1029/2007GL031361.

——, C. Schmitt, C.-C.-J. Chen, A. Bansemer, A. Gettelman, P. R. Field, and C. Liu, 2020: Contributions of the liquid and ice phases to global surface precipitation: Observations and global climate modeling. *J. Atmos. Sci.*, **77**, 2629–2648, https://doi.org/10.1175/JAS-D-19-0352.1.

Heymsfield, G. M., and Coauthors, 1996: The EDOP radar system on the high-altitude NASA ER-2 aircraft. *J. Atmos. Oceanic Technol.*, **13**, 795–809, https://doi.org/10.1175/1520-0426(1996)013<0795:TERSOT>2.0.CO;2.

Hobbs, P. V., S. Chang, and J. D. Locatelli, 1974: The dimensions and aggregation of ice crystals in natural clouds. *J. Geophys. Res.*, **79**, 2199–2206, https://doi.org/10.1029/JC079i015p02199.

Hou, A. Y., and Coauthors, 2014: The Global Precipitation Measurement Mission. *Bull. Amer. Meteor. Soc.*, **95**, 701–722, https://doi.org/10.1175/BAMS-D-13-00164.1.

Houze, R. A., and Coauthors, 2017: The Olympic Mountains Experiment (OLYMPEX). *Bull. Amer. Meteor. Soc.*, **98**, 2167–2188, https://doi.org/10.1175/BAMS-D-16-0182.1.

Iguchi, T., and Coauthors, 2018: GPM/DPR level-2 algorithm theoretical basis document. NASA Rep., 175 pp., https://pps.gsfc.nasa.gov/Documents/ATBD_DPR_202006_with_Appendix_a.pdf.

Jackson, R. C., G. M. McFarquhar, J. Stith, M. Beals, R. A. Shaw, J. Jensen, J. Fugal, and A. Korolev, 2014: An assessment of the impact of antishattering tips and artifact removal techniques on cloud ice size distributions measured by the 2D cloud probe. *J. Atmos. Oceanic Technol.*, **31**, 2567–2590, https://doi.org/10.1175/JTECH-D-13-00239.1.

Jensen, M. P., and Coauthors, 2016: The Midlatitude Continental Convective Clouds Experiment (MC3E). *Bull. Amer. Meteor. Soc.*, **97**, 1667–1686, https://doi.org/10.1175/BAMS-D-14-00228.1.

Kneifel, S., and D. Moisseev, 2020: Long-term statistics of riming in nonconvective clouds derived from ground-based doppler cloud radar observations. *J. Atmos. Sci.*, **77**, 3495–3508, https://doi.org/10.1175/JAS-D-20-0007.1.

——, M. S. Kulie, and R. Bennartz, 2011: A triple-frequency approach to retrieve microphysical snowfall parameters. *J. Geophys. Res.*, **116**, D11203, https://doi.org/10.1029/2010JD015430.

——, A. von Lerber, J. Tiira, D. Moisseev, P. Kollias, and J. Leinonen, 2015: Observed relations between snowfall microphysics and triple-frequency radar measurements. *J. Geophys. Res. Atmos.*, **120**, 6034–6055, https://doi.org/10.1002/2015JD023156.

Kollias, P., and B. Albrecht, 2005: Why the melting layer radar reflectivity is not bright at 94 GHz. *Geophys. Res. Lett.*, **32**, L24818, https://doi.org/10.1029/2005GL024074.

Kulie, M. S., and R. Bennartz, 2009: Utilizing spaceborne radars to retrieve dry snowfall. *J. Appl. Meteor. Climatol.*, **48**, 2564–2580, https://doi.org/10.1175/2009JAMC2193.1.

——, and L. Milani, 2018: Seasonal variability of shallow cumuliform snowfall: A *CloudSat* perspective. *Quart. J. Roy. Meteor. Soc.*, **144** (Suppl. 1), 329–343, https://doi.org/10.1002/qj.3222.

——, ——, N. B. Wood, S. A. Tushaus, R. Bennartz, and T. S. L'Ecuyer, 2016: A shallow cumuliform snowfall census using spaceborne radar. *J. Hydrometeor.*, **17**, 1261–1279, https://doi.org/10.1175/JHM-D-15-0123.1.

——, ——, ——, and T. S. L'Ecuyer, 2020: Global snowfall detection and measurement. *Satellite Precipitation Measurement*, Vol. 2, V. Levizzani et al., Eds., Springer, 699–716, https://doi.org/10.1007/978-3-030-35798-6_12.

Kuo, K. S., and Coauthors, 2016: Full access the microwave radiative properties of falling snow derived from nonspherical ice particle models. Part I: An extensive database of simulated pristine crystals and aggregate particles, and their scattering properties. *J. Appl. Meteor. Climatol.*, **55**, 691–708, https://doi.org/10.1175/JAMC-D-15-0130.1.

Leinonen, J., and W. Szyrmer, 2015: Radar signatures of snowflake riming: A modeling study. *Earth Space Sci.*, **2**, 346–358, https://doi.org/10.1002/2015EA000102.

——, and Coauthors, 2018: Retrieval of snowflake microphysical properties from multifrequency radar observations. *Atmos. Meas. Tech.*, **11**, 5471–5488, https://doi.org/10.5194/amt-11-5471-2018.

Li, L., G. M. Heymsfield, P. E. Racette, L. Tian, and E. Zenker, 2004: A 94-GHz cloud radar system on a NASA high-altitude ER-2 Aircraft. *J. Atmos. Oceanic Technol.*, **21**, 1378–1388, https://doi.org/10.1175/1520-0426(2004)021<1378:AGCRSO>2.0.CO;2.

——, and Coauthors, 2016: The NASA High-Altitude Imaging Wind and Rain Airborne Profiler. *IEEE Trans. Geosci. Remote Sens.*, **54**, 298–310, https://doi.org/10.1109/TGRS.2015.2456501.

Liu, G., 2009: Deriving snow cloud characteristics from *CloudSat* observations. *J. Geophys. Res.*, **114**, D00A09, https://doi.org/10.1029/2007JD009766.

Matrosov, S. Y., 2019: Comparative evaluation of snowfall retrievals from the *CloudSat* W-band radar using ground-based weather radars. *J. Atmos. Oceanic Technol.*, **36**, 101–111, https://doi.org/10.1175/JTECH-D-18-0069.1.

——, and A. Battaglia, 2009: Influence of multiple scattering on *CloudSat* measurements in snow: A model study. *Geophys. Res. Lett.*, **36**, L12806, https://doi.org/10.1029/2009GL038704.

McFarquhar, G. M., and Coauthors, 2017: Processing of ice cloud in situ data collected by bulk water, scattering, and imaging probes: Fundamentals, uncertainties, and efforts toward consistency. *Ice Formation and Evolution in Clouds and Precipitation: Measurement and Modeling Challenges*, *Meteor. Monogr.*, No. 58, Amer. Meteor. Soc., https://doi.org/10.1175/AMSMONOGRAPHS-D-16-0007.1.

McMurdie, L. A., and Coauthors, 2022: Chasing snowstorms: The Investigation Of Microphysics and Precipitation for Atlantic Coast-Threatening Snowstorms (IMPACTS) campaign. *Bull. Amer. Meteor. Soc.*, **103**, E1243–E1269, https://doi.org/10.1175/BAMS-D-20-0246.1.

Milani, L., and Coauthors, 2018: *CloudSat* snowfall estimates over Antarctica and the Southern Ocean: An assessment of independent retrieval methodologies and multi-year snowfall analysis. *Atmos. Res.*, **213**, 121–135, https://doi.org/10.1016/j.atmosres.2018.05.015.

Mróz, K., A. Battaglia, S. Kneifel, L. von Terzi, M. Karrer, and D. Ori, 2020: Linking rain into ice microphysics across the melting layer in stratiform rain: A closure study. *Atmos. Meas. Tech.*, **14**, 511–529, https://doi.org/10.5194/amt-14-511-2021.

——, M. Montopoli, A. Battaglia, G. Panegrossi, P. Kirstetter, and L. Baldini, 2021: Cross validation of active and passive microwave snowfall products over the continental United States. *J. Hydrometeor.*, **22**, 1297–1315, https://doi.org/10.1175/JHM-D-20-0222.1.

Norin, L., A. Devasthale, T. S. L'Ecuyer, N. B. Wood, and M. Smalley, 2015: Intercomparison of snowfall estimates derived from the *CloudSat* Cloud Profiling Radar and the ground-based weather radar network over Sweden. *Atmos. Meas. Tech.*, **8**, 5009–5021, https://doi.org/10.5194/amt-8-5009-2015.

Palerme, C., J. Kay, C. Genthon, T. L'Ecuyer, N. Wood, and C. Claud, 2014: How much snow falls on the Antarctic ice sheet? *Cryosphere*, **8**, 1577–1587, https://doi.org/10.5194/tc-8-1577-2014.

——, C. Genthon, C. Claud, J. E. Kay, N. B. Wood, and T. L'Ecuyer, 2017: Evaluation of current and projected Antarctic precipitation in CMIP5 models. *Climate Dyn.*, **48**, 225–239, https://doi.org/10.1007/s00382-016-3071-1.

Panegrossi, G., J.-F. Rysman, D. Casella, A. C. Marra, P. Sanò, and M. S. Kulie, 2017: *CloudSat*-based assessment of GPM microwave imager snowfall observation capabilities. *Remote Sens.*, **9**, 1263, https://doi.org/10.3390/rs9121263.

——, ——, ——, P. Sano, A. C. Marra, S. Dietrich, and M. S. Kulie, 2018: Exploitation of GPM/*CloudSat* coincidence dataset for global snowfall retrieval. *IGARSS 2018—2018 IEEE Int. Geoscience and Remote Sensing Symp.*, Valencia, Spain, Institute of Electrical and Electronics Engineers, 9323–9326, https://doi.org/10.1109/IGARSS.2018.8518297.

Petersen, W. A., P.-E. Kirstetter, J. Wang, D. B. Wolff, and A. Tokay, 2020: The GPM Ground Validation Program. *Satellite Precipitation Measurement*, Vol. 2, V. Levizzani et al., Eds., Springer, 471–502, https://doi.org/10.1007/978-3-030-35798-6_2.

Pettersen, C., and Coauthors, 2020: The Precipitation Imaging Package: Assessment of microphysical and bulk characteristics of snow. *Atmosphere*, **11**, 785, https://doi.org/10.3390/atmos11080785.

Rasmussen, R., and Coauthors, 2012: How well are we measuring snow: The NOAA/FAA/NCAR winter precipitation test bed. *Bull. Amer. Meteor. Soc.*, **93**, 811–829, https://doi.org/10.1175/BAMS-D-11-00052.1.

Rodgers, C. D., 2000: *Inverse Methods for Atmospheric Sounding: Theory and Practice*. Series on Atmospheric, Oceanic and Planetary Physics, Vol. 2, World Scientific, 256 pp.

Ryan, J. C., and Coauthors, 2020: Evaluation of *CloudSat*'s cloud-profiling radar for mapping snowfall rates across the Greenland Ice Sheet. *J. Geophys. Res. Atmos.*, **125**, e2019JD031411, https://doi.org/10.1029/2019JD031411.

Rysman, J.-F., G. Panegrossi, P. Sanò, A. Marra, S. Dietrich, L. Milani, and M. Kulie, 2018: SLALOM: An all-surface snow water path retrieval algorithm for the GPM Microwave Imager. *Remote Sens.*, **10**, 1278, https://doi.org/10.3390/rs10081278.

——, and Coauthor, 2019: Retrieving surface snowfall with the GPM Microwave Imager: A new module for the SLALOM

algorithm. *Geophys. Res. Lett.*, **46**, 13 593–13 601, https://doi.org/10.1029/2019GL084576.

——, C. Claud, and S. Dafis, 2021: Global monitoring of deep convection using passive microwave observations. *Atmos. Res.*, **247**, 105244, https://doi.org/10.1016/j.atmosres.2020.105244.

Sadowy, G., A. Berkun, W. Chun, E. Im, and S. Durden, 2003: Development of an advanced airborne precipitation radar. *Microwave J.*, **46**, 84–98.

Sassen, K., J. R. Campbell, J. Zhu, P. Kollias, M. Shupe, and C. Williams, 2005: Lidar and triple-wavelength doppler radar measurements of the melting layer: A revised model for dark- and brightband phenomena. *J. Appl. Meteor. Climatol.*, **44**, 301–312, https://doi.org/10.1175/JAM-2197.1.

——, S. Matrosov, and J. Campbell, 2007: *CloudSat* spaceborne 94 GHz radar bright bands in the melting layer: An attenuation-driven upside-down lidar analog. *Geophys. Res. Lett.*, **34**, L16818, https://doi.org/10.1029/2007GL030291.

Seto, S., T. Iguchi, and T. Oki, 2013: The basic performance of a precipitation retrieval algorithm for the global precipitation measurement mission's single/dual-frequency radar measurements. *IEEE Trans. Geosci. Remote Sens.*, **51**, 5239–5251, https://doi.org/10.1109/TGRS.2012.2231686.

——, ——, R. Meneghini, J. Awaka, T. Kubota, T. Masaki, and N. Takahashi, 2021: The precipitation rate retrieval algorithms for the GPM dual-frequency precipitation radar. *J. Meteor. Soc. Japan*, **99**, 205–237, https://doi.org/10.2151/jmsj.2021-011.

Skofronick-Jackson, G., and Coauthors, 2017: The Global Precipitation Measurement (GPM) mission for science and society. *Bull. Amer. Meteor. Soc.*, **98**, 1679–1695, https://doi.org/10.1175/BAMS-D-15-00306.1.

——, M. Kulie, L. Milani, S. J. Munchak, N. B. Wood, and V. Levizzani, 2019: Satellite estimation of falling snow: A Global Precipitation Measurement (GPM) *Core Observatory* perspective. *J. Appl. Meteor. Climatol.*, **58**, 1429–1448, https://doi.org/10.1175/JAMC-D-18-0124.1.

Souverijns, N., and Coauthors, 2018: Evaluation of the *CloudSat* surface snowfall product over Antarctica using ground-based precipitation radars. *Cryosphere*, **12**, 3775–3789, https://doi.org/10.5194/tc-12-3775-2018.

Stephens, G. L., and Coauthors, 2002: The *CloudSat* mission and the A-Train: A new dimension of space-based observations of clouds and precipitation. *Bull. Amer. Meteor. Soc.*, **83**, 1771–1790, https://doi.org/10.1175/BAMS-83-12-1771.

Tanelli, S., S. L. Durden, and E. Im, 2006: Simultaneous measurements of Ku- and Ka-band sea surface cross sections by an airborne radar. *IEEE Geosci. Remote Sens. Lett.*, **3**, 359–363, https://doi.org/10.1109/LGRS.2006.872929.

——, ——, ——, K. S. Pak, D. G. Reinke, P. Partain, J. M. Haynes, and R. T. Marchand, 2008: *CloudSat*'s cloud profiling radar after two years in orbit: Performance, calibration, and processing. *IEEE Trans. Geosci. Remote Sens.*, **46**, 3560–3573, https://doi.org/10.1109/TGRS.2008.2002030.

Tang, G., Y. Wen, J. Gao, D. Long, Y. Ma, W. Wan, and Y. Hong, 2017: Similarities and differences between three coexisting spaceborne radars in global rainfall and snowfall estimation. *Water Resour. Res.*, **53**, 3835–3853, https://doi.org/10.1002/2016WR019961.

Tridon, F., and Coauthors, 2019: The microphysics of stratiform precipitation during OLYMPEX: Compatibility between triple-frequency radar and airborne in situ observations. *J. Geophys. Res. Atmos.*, **124**, 8764–8792, https://doi.org/10.1029/2018JD029858.

Turk, F. J., 2016: *CloudSat*–GPM coincidence dataset: Version 1C. California Institute of Technology Jet Propulsion Laboratory Tech. Rep., 18 pp., https://gpm.nasa.gov/sites/default/files/document_files/CSATGPM_COIN_ATBD.pdf.

——, and Coauthors, 2021: Applications of a *CloudSat*–TRMM and *CloudSat*–GPM satellite coincidence dataset. *Remote Sens.*, **13**, 2264, https://doi.org/10.3390/rs13122264.

Tyynelä, J., J. Leinonen, D. Moisseev, and T. Nousiainen, 2011: Radar backscattering from snowflakes: Comparison of fractal, aggregate, and soft spheroid models. *J. Atmos. Oceanic Technol.*, **28**, 1365–1372, https://doi.org/10.1175/JTECH-D-11-00004.1.

Viviroli, D., R. Weingartner, and B. Messerli, 2003: Assessing the hydrological significance of the world's mountains. *Mt. Res. Dev.*, **23**, 32–40, https://doi.org/10.1659/0276-4741(2003)023[0032:ATHSOT]2.0.CO;2.

von Lerber, A., D. Moisseev, L. F. Bliven, W. Petersen, A. M. Harri, and V. Chandrasekar, 2017: Microphysical properties of snow and their link to *Ze–S* relations during BAECC 2014. *J. Appl. Meteor. Climatol.*, **56**, 1561–1582, https://doi.org/10.1175/JAMC-D-16-0379.1.

Wood, N. B., and T. S. L'Ecuyer, 2018: Level 2C snow profile process description and interface control document, product version P1_R05. NASA JPL CloudSat Project Doc. Rev. 0, 26 pp., https://www.cloudsat.cira.colostate.edu/cloudsat-static/info/dl/2c-snow-profile/2C-SNOW-PROFILE_PDICD.P1_R05.rev0_.pdf.

——, and ——, 2021: What millimeter-wavelength radar reflectivity reveals about snowfall: an information-centric analysis. *Atmos. Meas. Tech.*, **14**, 869–888, https://doi.org/10.5194/amt-14-869-2021.

——, ——, A. J. Heymsfield, and G. L. Stephens, 2015: Microphysical constraints on millimeter-wavelength scattering properties of snow particles. *J. Appl. Meteor. Climatol.*, **54**, 909–931, https://doi.org/10.1175/JAMC-D-14-0137.1.

Yin, M., and G. Liu, 2019: Assessment of GPM high-frequency microwave measurements with radiative transfer simulation under snowfall conditions. *Quart. J. Roy. Meteor. Soc.*, **145**, 1603–1616, https://doi.org/10.1002/qj.3515.

Yurkin, M. A., and A. G. Hoekstra, 2011: The discrete-dipole-approximation code ADDA: Capabilities and known limitations. *J. Quant. Spectrosc. Radiat. Transfer*, **112**, 2234–2247, https://doi.org/10.1016/j.jqsrt.2011.01.031.

Zhang, J., and Coauthors, 2011: National Mosaic and Multi-Sensor QPE (NMQ) System: Description, results, and future plans. *Bull. Amer. Meteor. Soc.*, **92**, 1321–1338, https://doi.org/10.1175/2011BAMS-D-11-00047.1.